ACS OMEGA

http://pubs.acs.org/journal/acsodf

Article

Role of Gallic Acid in the Synthesis of Carbon-Encapsulated Iron Nanoparticles by Hydrothermal Carbonization: Selecting Iron Oxide Composition

Rubén Correcher,* Yuriy Budyk, and Andrés Fullana

Cite This: *ACS Omega* 2021, 6, 29547−29554

Read Online

ACCESS | Metrics & More | Article Recommendations | Supporting Information

ABSTRACT: In this work, the role of phenolic compounds in the hydrothermal synthesis of carbon-encapsulated iron nanoparticles (CEINs) was studied. To model phenolic compounds, gallic acid (GA) was selected, with glucose as the carbon source. Iron was found as α-Fe_2O_3, γ-Fe_2O_3, Fe_3O_4, and zero-valent iron (ZVI) depending on the synthesis pH and GA/Fe molar ratio. For GA/Fe = 1, the CEINs' yield increased significantly. In the samples with phenolics, increasing the initial pH increased the amount of γ-Fe_2O_3 and Fe_3O_4 and enhanced the iron oxide encapsulation due to enhanced chelating ability. Reducing the GA/Fe ratio to 0.2 resulted in CEINs with stronger magnetization due to the presence of Fe_3O_4. Ash weight, HCl digestion, and Raman spectroscopy were used in conjunction to characterize the composition of the CEINs. The magnetization of the samples was compared using a simple magnetic weight setup. A scheme for the reactions occurring during the hydrothermal carbonization of GA−Fe complexes was proposed.

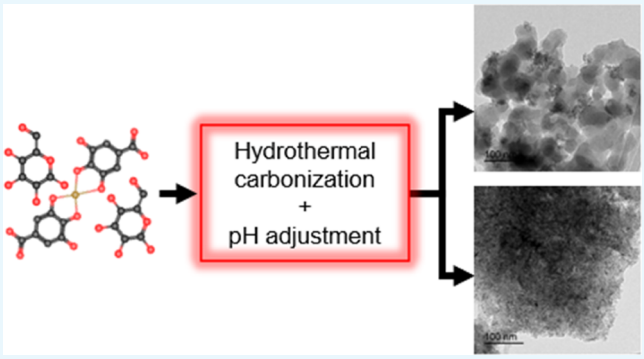

INTRODUCTION

Hydrothermal carbonization (HTC) reactions are being thoroughly investigated due to their ability to transform carbonaceous waste into higher-value products, such as hydrochar (HC) and biodiesel, using cheap catalysts while being environmentally benign.[1,2] In this process, wet biomass and liquid waste rich in dissolved carbon are subjected to temperatures higher than 100 °C in a sealed reactor that can sustain the autogenous pressure. As a result, the carbon can turn into gaseous, liquid, and solid products. During HTC, hydrocarbons initially undergo many chemical reactions (dehydration, hydrolysis, etc.), turning into simpler molecules and organic acids. In the case of saccharides, the main products are organic acids and furfural compounds (FCs).[3] FCs act as structural units, condensing and polymerizing under hydrothermal conditions, resulting in an amorphous carbon matrix that grows into carbon microspheres. Iron salts are known to catalyze this reaction, enhancing the dehydration of saccharides and the production of FCs even at low temperatures.[4,5] When iron salts are added, they precipitate into oxides and ZVI, which are incorporated into the carbon matrix. These are known as carbon-encapsulated iron nanoparticles (CEINs).

CEINs are a promising catalyst in fuel technology and environmental remediation. Obtaining cheap catalysts for the Fischer−Tropsch synthesis (FTS) is paramount to escalate synthetic fuel production.[6,7] Yu et al. were the first to study the viability of CEINs synthesized from HTC for the hydrogenation of CO. These were synthesized from cheap reagents, glucose as the carbonaceous source, and iron nitrate as the catalyst for carbonization.[4] The carbon matrix of the CEINs prevented aggregation of the metal species, and their small size resulted in high CO conversion rates even after a long treatment time. The chemistry of the carbon matrix also has a strong impact on catalytic behavior. Guo et al. synthesized N-doped CEINs with different nitrogenated reagents under mild hydrothermal conditions (150 °C) and found that the catalytic activity toward CO_2 hydrogenation depended heavily on the N precursor.[8] Recently, CEINs have also been employed in microbial fuel cells, obtaining a 50% increase in power density compared to expensive Pt/C-based electrocatalysts.[9] In environmental remediation, CEINs combine the reducing capabilities of metallic iron due to its ZVI content and enhanced adsorption due to the carbon surface chemistry.[10,11] Calderon et al. studied the hydrothermal synthesis of CEINs using olive mill wastewater (OMW) and iron nitrate.[12] These were compared to CEINs synthesized with glucose and iron nitrate. OMW has a high content of metal-chelating

Received: July 13, 2021
Accepted: September 28, 2021
Published: October 26, 2021

polyphenols. After the introduction of iron nitrate, the polyphenols formed iron chelates. Their carbonization resulted in CEINs with higher ZVI and oxide content. The morphology was also different from the typical microspheres obtained from glucose. Instead, CEINs from OMW formed agglomerated nanospheres. This different morphology granted a higher surface area. The CEINs were used for the sequestration of heavy metal cations, where the carbon shell prevented the release of contaminants. To further increase the surface area and ZVI content, CEINs are activated via pyrolysis under an inert atmosphere, reducing the oxides encapsulated to metallic iron due to carbothermal reduction. CEINs and activated CEINs (a-CEINs) have been used to remediate heavy metals and organic contaminants. While a-CEINs have greater sorption capabilities, the synthesis requires high temperatures (550−900 °C) and they have lower regeneration capabilities.[13] Activation can be detrimental for the sequestration of heavy metals since the presence of amorphous carbon and iron oxides in the CEINs' surface facilitates the adsorption of metal cations.[12,14] CEINs can have appreciable magnetization due to their metal content, which allows for facile extraction after remediation. The composition of CEINs is of great importance for their area of application: small iron oxides are required for high activity in FTS synthesis while a high content of ZVI is necessary for the effective reduction of organic pollutants.

CEINs can be synthesized from diverse carbonaceous precursors and iron salts with different results depending on the conditions and post-treatment.[15,16] Both phenolic compounds and iron salts are catalysts that modify the products of HTC.[17,18] Phenolic compounds with specific ligand configurations can bind to transition metal ions, creating a ligand to metal charge transfer (LMCT) complex. These complexes are characterized by their strong molar absorptivity, which gives them an intense coloration depending on the number of molecules forming the complex. The more common ligands involved in the metal-binding process are adjacent *ortho*-hydroxyl (−OH) groups although other ligands might also be involved when various phenolic compounds are present.[19] For binding to take place, the chelating ligand must be deprotonated, meaning that the process heavily depends on the pH. The GA molecule can chelate Fe through −COOH (pK_a = 4.5) and −OH (pK_a = 10) groups.

Other chelating agents such as EDTA, citric acid, and tannic acid have been used in the past to synthesize CEINs and other nanomaterials, but GA has not been used yet in the HTC synthesis of CEINs.[20−22] This work aims to study the role of phenolics in the HTC synthesis of CEINs using a ferric salt and a solution of glucose with GA. GA was chosen as a model phenolic compound due to its wide presence in plant-based biomass and its ability to form iron complexes.[23,24] Through adjustment of the initial pH, the −COOH and −OH groups of GA were deprotonated, altering polymerization and ultimately the CEIN yield, morphology, and composition.

■ ANALYSIS AND METHODS

The mass of iron species encapsulated in the CEINs was measured by the ash weight. To obtain the ashes, a quantity of at least 150 mg of CEINs was heated in air at 950 °C for 3 h to volatilize their HC content. The resulting ashes were Fe_2O_3 from the encapsulated iron species. A blank sample of HC from glucose and GA was treated in the same manner to find if other inorganics were present in the ash. No ashes were found for these samples, indicating that Fe_2O_3 was the only ash material. To assess the ZVI content, the CEINs were digested in HCl in a sealed vessel. The increase in pressure due to the generation of hydrogen gas (as follows in eq 1) was used to estimate the ZVI through the ideal gas law.[12] In the procedure, 0.2 g of CEINs was introduced in 120 mL glass bottles. Then, 5 mL of 37% HCl was rapidly introduced, and the bottles were sealed immediately with a septum. The mixtures were left to react for 2 h for a complete reaction. Then, the pressure generated was measured with a digital pressure meter with a needle by perforating the septum. The pressures generated ranged from 40 to 100 mbar. The measurements were performed in duplicate, and the mean was used.

$$2Fe(s) + 6HCl(l) \rightarrow 2FeCl_3(aq) + 3H_2(g) \quad (1)$$

The ZVI content was subtracted from the ashes, leading to the iron oxide content. From this data, the mass percentage of HC (%HC), iron species (%Fe), iron oxides (%Ox), and ZVI (%ZVI) of the CEINs were calculated. The quantities follow eqs 2 and 3.

$$100\% = \%HC + \%Fe \quad (2)$$

$$\%Fe = \%Ox + \%ZVI \quad (3)$$

The yield of CEINs (Y_{CEINs}) was calculated using eq 4, where $m_{Glucose}$ and m_{GA} are the mass of D-Glucose and GA, respectively, m_{Fe} is the mass of iron in the iron nitrate, and m_{CEINs} is the dry mass of CEINs.

$$Y_{CEINs} = \frac{m_{CEINs}}{m_{Glucose} + m_{GA} + m_{Fe}} \quad (4)$$

The phases of the iron oxides were identified via dispersive Raman spectroscopy using a LabRam (Jobin-Ivon) spectrometer with a 632 nm laser. Iron oxides present active vibrational modes between 200 and 1000 cm^{-1} (Table S1). These can be used to distinguish the iron oxide phases despite their low crystallinity in the CEINs. The oxide peaks were fitted to those found in the work of Testa-Anta et al.[25] The carbon peaks from these samples were compared for insight into the HC structure of the CEINs (Table S2).

A JEOL JEM-1400 Plus was used to acquire TEM images of the CEINs and the encapsulated iron species. A comparative measure of magnetization was obtained using a magnetic weight setup.[26] In short, a sample holder above and separated from the balance was filled with a mass of CEINs. In contact with the balance, a holder with a magnet could be lifted or lowered with a lever. The magnet was situated between the CEINs and high enough so that the magnetic field would not interfere with the balance. The relationship between magnetization and force is described in eq 5.

$$\sigma = \frac{F_z}{m_s \nabla B_z}, \; F_z = \Delta m \cdot g \quad (5)$$

where σ (emu/kg) is the mass magnetization of the sample, F_z (N) is the magnet weight, Δm (kg) is the mass change due to the pull exerted by the CEINs to the magnet, ∇B_z (T/m) is the magnetic field gradient of the magnet in the z-direction, and m_s (kg) is the CEINs' sample mass. Comparisons were drawn using the mass normalized force exerted at a certain distance, $(\Delta m/m_s)_d$. The measurements were carried out with the least amount of CEINs possible to avoid artifacts arising from the geometry and always using the same ∇B_z. The maximum standard error was 6% at the minimum distance. This error can be reduced with better control of the distance between the

https://doi.org/10.1021/acsomega.1c03692
ACS Omega 2021, 6, 29547−29554

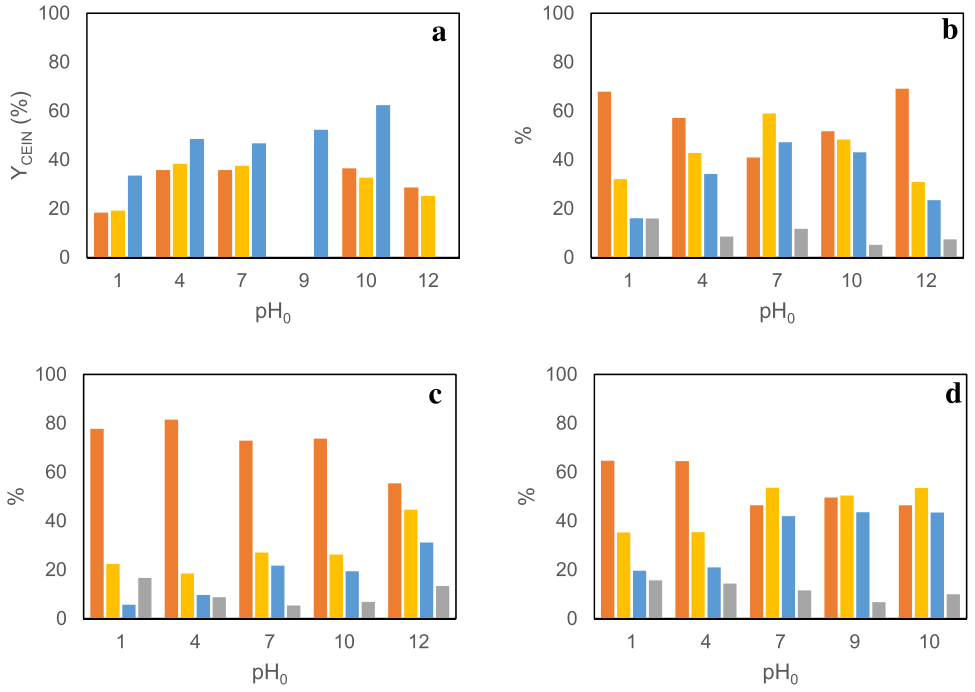

Figure 1. (a) Y_{CEIN} for C_0 (orange), $C_{0.2}$ (yellow), and C_1 (blue). %HC (orange), %Fe (yellow), %Ox (blue), and %ZVI (gray) for batches C_0 (b), $C_{0.2}$ (c), and C_1 (d).

magnet and the sample. In any case, the purpose was to provide a quick visual representation of the magnetization of the CEINs.

RESULTS AND DISCUSSION

CEINs' Yield and Ultimate Analysis. For samples C_{0-1} and C_{0-4}, iron was initially present as aqueous Fe^{3+}. Due to the pH_0 adjustment, Fe^{3+} precipitated into $Fe(OH)_3$ for samples C_{0-7}, C_{0-10}, and C_{0-12}. During HTC, glucose decomposed into FCs and organic acids, reducing the pH below 7. This results in the redissolution of $Fe(OH)_3$ into Fe^{3+} for samples C_{0-7}, C_{0-10}, and C_{0-12}. The FCs polymerized incorporating a fraction of the total Fe^{3+} introduced. Figure 1a shows that Y_{CEIN} was higher between pH_0 4 and 10. Also, Figure 1b shows that %HC and %Fe were minimum and maximum between pH_0 7 and 10. The production of FCs from saccharides depends strongly on the pH_0 and the presence of heterogeneous catalysts.[27,28] The decrease of Y_{CEIN} beyond pH_0 10 is due to a reduction in the production of FCs that would produce the CEINs.

Introducing Fe^{3+} into a GA solution leads to the formation of GA−Fe complexes. These complexes retain Fe^{3+} in the whole pH_0 range, inhibiting the precipitation of $Fe(OH)_3$. As seen in Figure 1a, the Y_{CEIN} values for batch $C_{0.2}$ were similar to those of batch C_0 at each pH_0. Due to the low GA/Glucose ratio (0.06), the production of CEINs was still highly dependent on the production of FCs. Despite this, the addition of GA resulted in different %HC and %Fe trends with pH_0. For batch C_0, %HC diminished and %Fe increased toward pH_0 7, while for batch $C_{0.2}$ %HC diminished and %Fe increased with higher pH_0 (Figure 1b,c). The decrease of %HC and increase of %Fe in batch $C_{0.2}$ were more significant between pH_0 4 and 7 and pH_0 10 and 12. These ranges of pH correspond to the deprotonation of −COOH (pK_a = 4.5) and −OH (pK_a = 10) from GA. After deprotonation, these groups can chelate and incorporate more Fe^{3+}, resulting in lower %HC and higher %Fe.

For batch C_1, the GA/Glucose ratio was higher (0.33) and GA had a stronger influence in polymerization, resulting in increased Y_{CEIN} at higher pH_0. %HC decreased and %Fe increased from pH_0 4 to 7, but no significant changes were observed at higher pH_0 (Figure 1d).

The %Ox content followed a behavior similar to %Fe in all batches. In contrast, a trend for %ZVI was hard to discern, with the only similarity being that %ZVI was always the maximum at pH_0 1. ZVI appears due to the reduction of Fe^{3+} to Fe^0. This has been seen in the synthesis of ZVI nanoparticles using plant extracts with a high content of phenolics, which also act as stabilizers.[29,30] Since GA is unable to completely reduce Fe^{3+}, the hydrothermal degradation of D-glucose must produce chemicals that are able to perform this reduction. The production of these chemicals would be higher at lower pH_0, explaining the %ZVI maximums at pH_0 1. However, to confirm the production of stronger reducing organic compounds, further analysis of the HTC liquor would be required.

Characterization of CEINs. Apart from the mass composition, it was observed that the samples $C_{0.2-7}$, $C_{0.2-10}$, and especially $C_{0.2-12}$ were magnetic. Raman spectroscopy was used to study the metal oxide content in the batch with a GA/Fe ratio of 0.2. From these results, the iron oxides produced during HTC of Fe−GA complexes were obtained. The spectra obtained also allowed the study of the carbonaceous matrix of the CEINs. The iron oxide phases found were α-Fe_2O_3, γ-Fe_2O_3, and Fe_3O_4. Samples C_{0-12} and C_{1-10} were also studied for comparison (Figure S1). The composition of the iron oxides is presented in Table 1.

The samples with a GA/Fe ratio of 0.2 all presented similar quantities of α-Fe_2O_3 except for $C_{0.2-12}$, which had none. For these samples, the GA reduced part of the Fe^{3+} to Fe^{2+} resulting in the precipitation of Fe_3O_4 nanoparticles. These would gradually oxidate into γ-Fe_2O_3 due to the presence of O_2

https://doi.org/10.1021/acsomega.1c03692
ACS Omega 2021, 6, 29547−29554

Table 1. Iron Oxide Composition of CEINs

sample	α-Fe_2O_3	γ-Fe_2O_3	Fe_3O_4
C_{0-12}	100	0	0
$C_{0.2-4}$	45.1	43	11.9
$C_{0.2-7}$	42.1	30.9	27
$C_{0.2-10}$	42.2	34.3	23.5
$C_{0.2-12}$	0	43.9	56.1
C_{1-10}	0	100	0

and hydrothermal conditions. At pH <7, part of the Fe^{3+} of the γ-Fe_2O_3 would dissolve back into solution, later precipitating as α-Fe_2O_3 due to the hydrothermal conditions. This is also the case for sample C_{0-12}, where Fe^{3+} from solution, or from dissolution of $Fe(OH)_3$ precipitates as α-Fe_2O_3. This mechanism has already been studied with Fe_3O_4 microparticles.[31] In sample $C_{0.2-12}$, the pH > 7 during the reaction disabled the oxidative pathway into α-Fe_2O_3. This also occurs for sample C_{1-10}, where all of the iron oxide is γ-Fe_2O_3 due to complete oxidation of Fe_3O_4.

The carbonaceous matrix was studied deconvoluting the Raman spectra between 1000 and 1800 cm^{-1} (Figure S2). Three bands were identified: D (~1350 cm^{-1}), A (~1500 cm^{-1}), and G (~1580 cm^{-1}). The D band corresponds to disordered graphitic lattices, the A band to amorphous carbon, and the G band to the ideal graphitic lattice.[32,33] The shape of the spectra varied notably with the pH_0 used. The intensity ratio of the A band and G band (I_A/I_G) is deemed as a good indicator of the amount of amorphous carbon in soot and carbon black.[33] Figure S3 shows that I_A/I_G followed a linear increase in this ratio beyond pH_0 7, indicating that the amorphous carbon content increased with pH_0.

TEM images were used for further insight into the structural changes. The blank sample consisted of interconnected carbon nanochains and carbon microspheres (Figure 2a,b) corresponding to HTC of GA and FCs, respectively. Using only

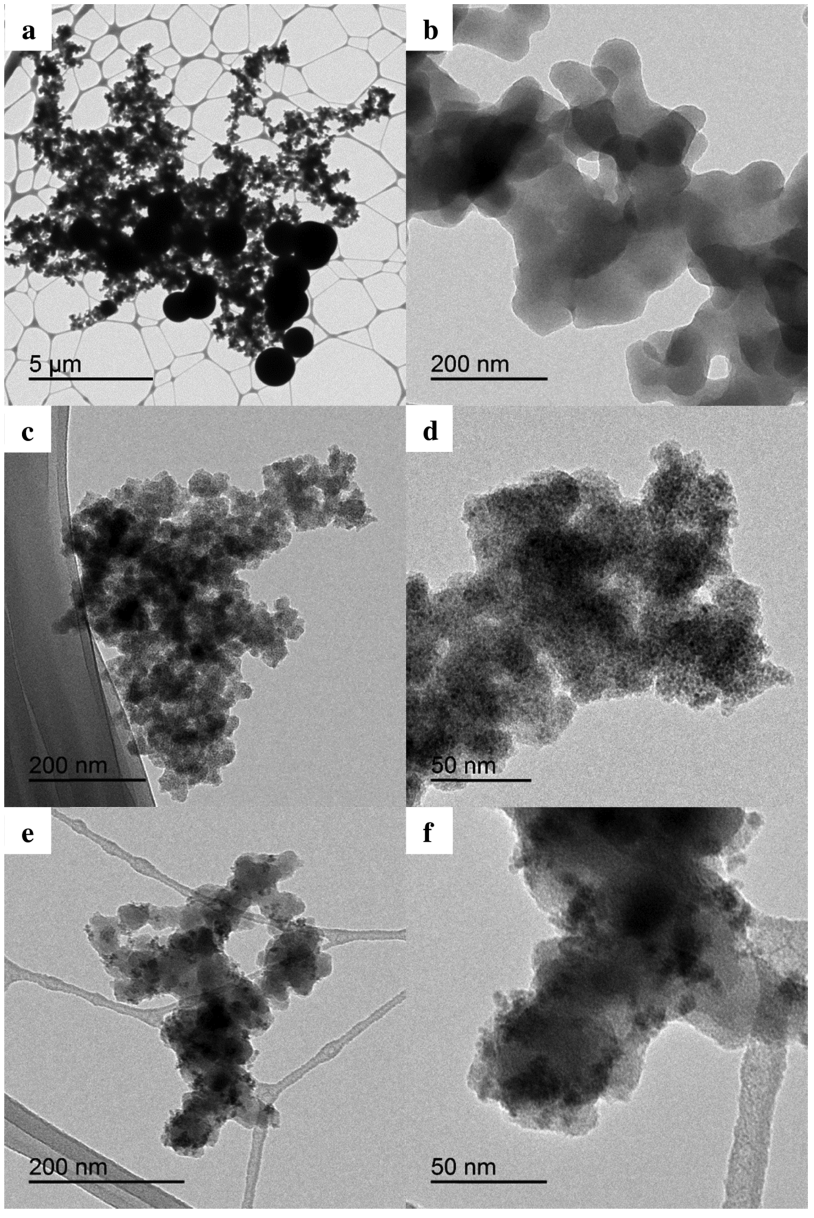

Figure 2. TEM images of the (a, b) blank, (c, d) C_{0-12}, and (e, f) $C_{0.2-4}$.

https://doi.org/10.1021/acsomega.1c03692
ACS Omega 2021, 6, 29547−29554

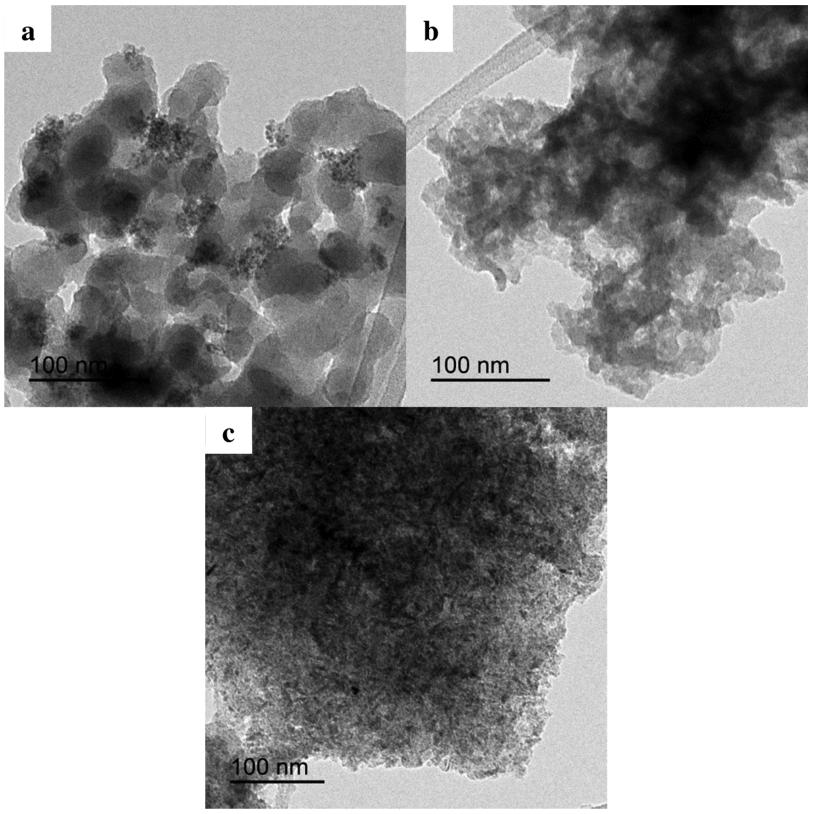

Figure 3. TEM images of samples (a) $C_{0.2-7}$, (b) $C_{0.2-10}$, and (c) $C_{0.2-12}$. The features between change significantly with pH_0.

Scheme 1. Reactions during HTC of a Carbonaceous Precursor with and without GA. Iron Will Be Initially Present in Different Forms Depending on the Presence of Phenolics and the Initial pH

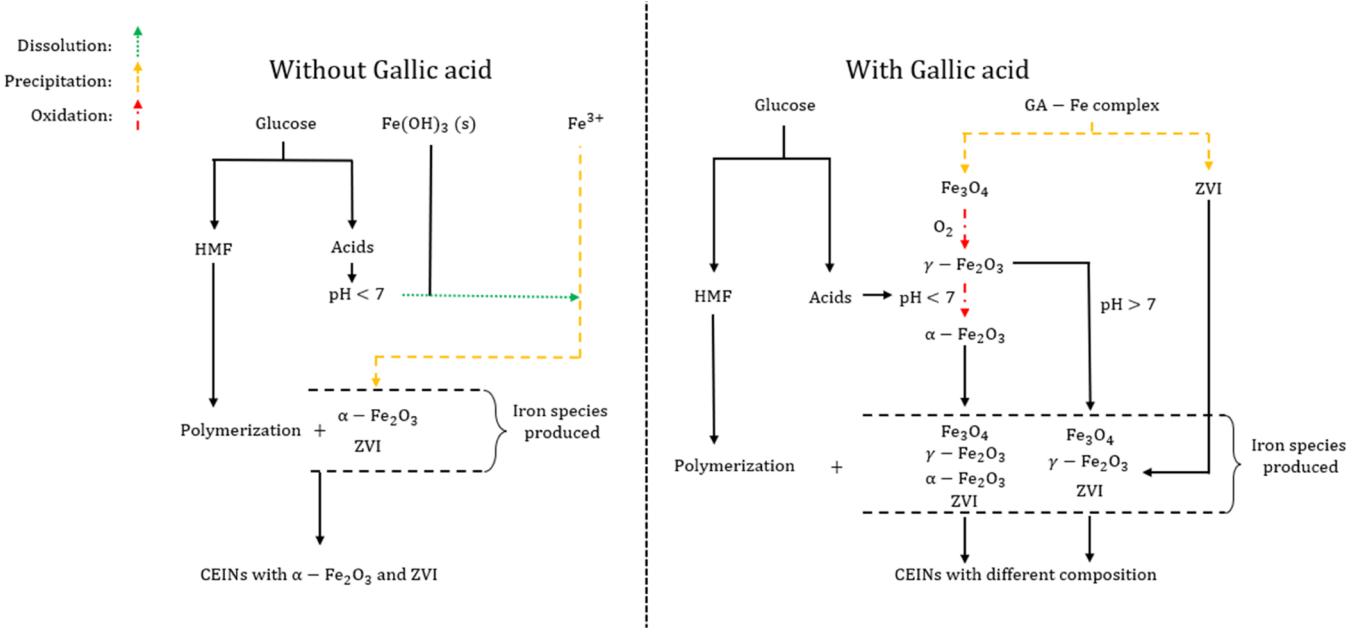

glucose and iron nitrate at pH_0 12 led to smaller chains filled with α-Fe_2O_3 and ZVI instead of the usual carbon microspheres (Figure 2c,d). Combining GA, glucose, and iron nitrate resulted in a mixture of these two structures: carbon nanochains with agglomerated metal oxides and ZVI (Figure 2e,f). Increasing pH_0 led to a progressive shrinkage and aggregation of the carbon nanochains, finally creating highly packed CEINs at pH_0 12 (Figure 3a−c). The difference in packing behavior resulted from having a higher quantity of deprotonated ligands at higher pH. In conjunction with Raman analysis, we confirm that the GA/Fe ratio and pH_0 have a substantial effect on the formation of the CEINs.

Finally, a homemade magnetic weight system was used to study the magnetization of the samples with a GA/Fe ratio of

https://doi.org/10.1021/acsomega.1c03692
ACS Omega 2021, 6, 29547−29554

0.2. An exponential increase in magnetization occurs for the experiment at pH_0 12 (Figure S4). A possible explanation for this increase is the formation of tightly packed Fe_3O_4 in the amorphous carbon matrix (Figure 3c). The packing results in an increased density of magnetically coupled Fe_3O_4 nanoparticles, which would behave as single magnetic domains under a magnetic field.[34,35] The lack of α-Fe_2O_3 would also facilitate the formation of such domains.

Based on these results, two different pathways for the formation of CEINs are proposed (Scheme 1). When saccharides are present, the iron is present as either Fe^{3+} or precipitated $Fe(OH)_3$, depending on the pH_0. During the first stage of HTC, the saccharides degrade producing FCs and organic acids that acidify the solution (if pH_0 is above 3). Following, the FCs start polymerizing, while the Fe^{3+} precipitates or $Fe(OH)_3$ dehydrates into α-Fe_2O_3. The α-Fe_2O_3 is integrated into the carbon microspheres forming CEINs. A fraction of Fe^{3+} is reduced to Fe^0, resulting in ZVI in the CEINs. For GA and other simple polyphenols, Fe^{3+} is chelated, forming GA−Fe complexes. Depending on the pH_0, carboxylic and hydroxylic groups deprotonate, opening different paths to chelate Fe^{3+} and polymerization. During HTC, the chelated iron precipitates as Fe_3O_4 due to reduction to Fe^{2+} in the GA−Fe complex. These precipitates are encapsulated by GA molecules that polymerize, finally forming the CEINs. During HTC, the high temperature and aerobic environment result in the partial or complete oxidation of Fe_3O_4 into γ-Fe_2O_3. If the pH during HTC was below 7, γ-Fe_2O_3 could dissolve as Fe^{3+} and later precipitate as α-Fe_2O_3 in the CEINs. Similarly, ZVI was also found in these CEINs.

CONCLUSIONS

The HTC of a solution comprising glucose and iron nitrate and different ratios of GA/Fe and pH_0 were used to explore the changes brought by the presence of phenolic compounds in the synthesis of CEINs. The procedure allowed the synthesis of CEINs containing different iron oxides by tuning the GA/Fe molar ratio and pH_0 while maintaining an equal treatment time and temperature. The morphology, structure, and magnetic properties of the CEINs were also severely affected by these parameters. These changes were attributed to the quantity of available ligands for chelation and polymerization. A scheme for the different reactions occurring during HTC of GA−Fe complexes was drawn. The differences in iron loading are significant in the activation process of the CEINs for the synthesis of FTS catalysts. Also, the different morphologies and magnetic behavior might be of interest for contaminant remediation.

EXPERIMENTAL SECTION

Reagents. Chemical reagents used were D-glucose ($C_6H_{12}O_6$, Merck, 99.5%), gallic acid ($C_7H_6O_5$, Sigma-Aldrich, 97.5%), iron nitrate nonahydrate ($Fe(NO_3)_3{\cdot}9H_2O$, Fischer Chemical, 99.1%), sodium hydroxide (NaOH, Fischer Chemical, 97%), and 37% hydrochloric acid (HCl, Labkem). The solutions were prepared using deionized water.

CEIN Synthesis. In a beaker with 30 mL of deionized water, glucose (16.6 or 8.3 mmol) and GA (2.8 or 1 mmol) were stirred until complete dissolution. The samples without GA used 16.6 mmol glucose. Afterward, iron (III) nitrate nonahydrate (4.3, 4, or 2.8 mmol) was introduced, which turned the transparent solution into a dark purple color. Then, the solution pH was adjusted using a 20% (w/v) NaOH solution, if required. The volumes were increased to 50 mL, and the solutions were introduced into 80 mL Teflon-lined autoclave reactors and sealed. The autoclaves were then heated to 180 °C for 5 h maintaining the autogenous pressure in a furnace to perform the HTC. After treatment, the autoclaves were left to cool overnight. The contents were vacuum filtered with 5−13 μm qualitative filter paper (VWR) and thoroughly washed with deionized water and methanol. The supernatant was stored to measure the final pH of the solution. The solid product was dried under aerobic conditions in a furnace for 12 h at 60 °C. Afterward, the remaining solids were crushed in a mortar, obtaining a fine black powder. Table 2 presents the GA concentrations (C_{GA}) and molar ratios used. The iron-to-carbon molar ratio (Fe/C) was constant to ensure that possible changes in the yield and morphology were due to the GA and iron content. The molar carbon included both carbons from glucose and GA. The samples were named after their GA/Fe molar ratio (X) and initial pH (Y) (C_{X-Y}). A blank was prepared using a glucose and GA solution. For batch C_1, the higher pH was limited to 10 to avoid fouling of the CEINs. Another point (pH 9) was taken instead. Sample C_{1-9} had very fine CEINs in solution. To recuperate them, the contents of the autoclave were first completely dried at 90 °C. Then, the remaining solid was washed with methanol and vacuum filtered in the same conditions. The powders were stored for further analysis.

Table 2. GA Concentration and Iron-to-Carbon (Fe/C), GA-to-Iron (GA/Fe), and GA-to-Glucose (Ga/Glu) Molar Ratios

sample	C_{GA} (mM)	Fe/C	GA/Fe	GA/Glu
blank	20	0		0.06
C_{0-1}	0	0.04	0	0
C_{0-4}				
C_{0-7}				
C_{0-10}				
C_{0-12}				
$C_{0.2-1}$	20	0.04	0.2	0.06
$C_{0.2-4}$				
$C_{0.2-7}$				
$C_{0.2-10}$				
$C_{0.2-12}$				
C_{1-1}	56	0.04	1	0.33
C_{1-4}				
C_{1-7}				
C_{1-9}				
C_{1-10}				

ASSOCIATED CONTENT

Supporting Information

The Supporting Information is available free of charge at https://pubs.acs.org/doi/10.1021/acsomega.1c03692.

Raman spectra and deconvolution of samples C_{0-12}, $C_{0.2-4}$ to $C_{0.2-12}$, and C_{1-10} between 200 and 800 cm^{-1} (Figure S1); Raman spectra and deconvolution of samples $C_{0.2-4}$ to $C_{0.2-12}$ between 1000 and 1800 cm^{-1} (Figure S2); dependence between pH_0 and I_A/I_G ratios obtained from Raman spectra of samples $C_{0.2-4}$ to $C_{0.2-12}$ between 1000 and 1800 cm^{-1} (Figure S3); and comparison of magnetization measured with a magnetic

https://doi.org/10.1021/acsomega.1c03692
ACS Omega 2021, 6, 29547−29554

weight for samples C_{0-12}, C_{1-10}, and $C_{0.2-4}$ to $C_{0.2-12}$ (Figure S4). Peak data extracted from the Raman spectra between 200 and 800 cm^{-1} for C_{0-12}, $C_{0.2-4}$ to $C_{0.2-12}$, and C_{1-10} (Table S1) and peak data extracted from the Raman spectra between 1000 and 1800 cm^{-1} for $C_{0.2-4}$ to $C_{0.2-12}$ (Table S2) (PDF)

AUTHOR INFORMATION

Corresponding Author

Rubén Correcher − *Department of Chemical Engineering, Institute University of Water and Environmental Sciences, University of Alicante, 03690 Alicante, Spain;* orcid.org/0000-0002-3243-7157; Phone: +34965903400; Email: ruben.gc@ua.es

Authors

Yuriy Budyk − *Department of Chemical Engineering, Institute University of Water and Environmental Sciences, University of Alicante, 03690 Alicante, Spain;* orcid.org/0000-0001-8734-2801

Andrés Fullana − *Department of Chemical Engineering, Institute University of Water and Environmental Sciences, University of Alicante, 03690 Alicante, Spain;* orcid.org/0000-0002-6883-3215

Complete contact information is available at: https://pubs.acs.org/10.1021/acsomega.1c03692

Notes

The authors declare no competing financial interest.

REFERENCES

(1) Shen, Y. A Review on Hydrothermal Carbonization of Biomass and Plastic Wastes to Energy Products. *Biomass and Bioenergy*; Elsevier Ltd., 2020; p 105479.

(2) Beims, R. F.; Hu, Y.; Shui, H.; Xu, C. Charles. Hydrothermal Liquefaction of Biomass to Fuels and Value-Added Chemicals: Products Applications and Challenges to Develop Large-Scale Operations. *Biomass and Bioenergy*; Elsevier Ltd., 2020; p 105510.

(3) Sevilla, M.; Fuertes, A. B. Chemical and Structural Properties of Carbonaceous Products Obtained by Hydrothermal Carbonization of Saccharides. *Chem. - Eur. J.* **2009**, *15*, 4195−4203.

(4) Yu, G.; Sun, B.; Pei, Y.; Xie, S.; Yan, S.; Qiao, M.; Fan, K.; Zhang, X.; Zong, B. FexOy@C Spheres as an Excellent Catalyst for Fischer-Tropsch Synthesis. *J. Am. Chem. Soc.* **2010**, *132*, 935−937.

(5) Cui, X.; Antonietti, M.; Yu, S.-H. Structural Effects of Iron Oxide Nanoparticles and Iron Ions on the Hydrothermal Carbonization of Starch and Rice Carbohydrates. *Small* **2006**, *2*, 756−759.

(6) Li, X.; Anderson, P.; Jhong, H. R. M.; Paster, M.; Stubbins, J. F.; Kenis, P. J. A. Greenhouse Gas Emissions, Energy Efficiency, and Cost of Synthetic Fuel Production Using Electrochemical CO2 Conversion and the Fischer-Tropsch Process. *Energy Fuels* **2016**, *30*, 5980−5989.

(7) Snehesh, A. S.; Mukunda, H. S.; Mahapatra, S.; Dasappa, S. Fischer-Tropsch Route for the Conversion of Biomass to Liquid Fuels - Technical and Economic Analysis. *Energy* **2017**, *130*, 182−191.

(8) Guo, L.; Zhang, P.; Cui, Y.; Liu, G.; Wu, J.; Yang, G.; Yoneyama, Y.; Tsubaki, N. One-Pot Hydrothermal Synthesis of Nitrogen Functionalized Carbonaceous Material Catalysts with Embedded Iron Nanoparticles for CO 2 Hydrogenation. *ACS Sustainable Chem. Eng.* **2019**, *7*, 8331−8339.

(9) Fan, Z.; Li, J.; Yang, W.; Fu, Q.; Sun, K.; Song, Y. C.; Wei, Z.; Liao, Q.; Zhu, X. Green and Facile Synthesis of Iron Oxide Nanoparticle-Embedded N-Doped Biocarbon as an Efficient Oxygen Reduction Electrocatalyst for Microbial Fuel Cells. *Chem. Eng. J.* **2020**, *385*, No. 123393.

(10) Li, X. Q.; Elliott, D. W.; Zhang, W. X. Zero-Valent Iron Nanoparticles for Abatement of Environmental Pollutants: Materials and Engineering Aspects. *Crit. Rev. Solid State Mater. Sci.* **2006**, *31*, 111−122.

(11) Bonaiti, S.; Calderon, B.; Collina, E.; Lasagni, M.; Mezzanotte, V.; Aracil, I.; Fullana, A. In *Nitrogen Activation of Carbon-Encapsulated Zero-Valent Iron Nanoparticles and Influence of the Activation Temperature on Heavy Metals Removal*, IOP ConferenceSeries: Earth and Environmental Science; Institute of Physics Publishing, 2017; Vol. 64, p 12070.

(12) Calderon, B.; Smith, F.; Aracil, I.; Fullana, A. Green Synthesis of Thin Shell Carbon-Encapsulated Iron Nanoparticles via Hydrothermal Carbonization. *ACS Sustainable Chem. Eng.* **2018**, *6*, 7995−8002.

(13) Strachowski, P.; Bystrzejewski, M. Comparative Studies of Sorption of Phenolic Compounds onto Carbon-Encapsulated Iron Nanoparticles, Carbon Nanotubes and Activated Carbon. *Colloids Surf., A* **2015**, *467*, 113−123.

(14) Pyrzyńska, K.; Bystrzejewski, M. Comparative Study of Heavy Metal Ions Sorption onto Activated Carbon, Carbon Nanotubes, and Carbon-Encapsulated Magnetic Nanoparticles. *Colloids Surf., A* **2010**, *362*, 102−109.

(15) Sun, H.; Zhou, G.; Liu, S.; Ang, H. M.; Tadé, M. O.; Wang, S. Nano-Fe0 Encapsulated in Microcarbon Spheres: Synthesis, Characterization, and Environmental Applications. *ACS Appl. Mater. Interfaces* **2012**, *4*, 6235−6241.

(16) Yan, Q.; Street, J.; Yu, F. Synthesis of Carbon-Encapsulated Iron Nanoparticles from Wood Derived Sugars by Hydrothermal Carbonization (HTC) and Their Application to Convert Bio-Syngas into Liquid Hydrocarbons. *Biomass and Bioenergy* **2015**, *83*, 85−95.

(17) Ryu, J.; Suh, Y. W.; Suh, D. J.; Ahn, D. J. Hydrothermal Preparation of Carbon Microspheres from Mono-Saccharides and Phenolic Compounds. *Carbon* **2010**, *48*, 1990−1998.

(18) Saadattalab, V.; Wang, X.; Szego, A. E.; Hedin, N. Effects of Metal Ions, Metal, and Metal Oxide Particles on the Synthesis of Hydrochars. *ACS Omega* **2020**, *5*, 5601−5607.

(19) Hider, R. C.; Liu, Z. D.; Khodr, H. H. Metal Chelation of Polyphenols. *Methods Enzymol.* **2001**, *335*, 190−203.

(20) Chirita, M.; Ieta, A. FeCO3 Microparticle Synthesis by Fe-EDTA Hydrothermal Decomposition. *Cryst. Growth Des.* **2012**, *12*, 883−886.

(21) Behdadfar, B.; Kermanpur, A.; Sadeghi-Aliabadi, H.; Morales, M. D. P.; Mozaffari, M. Synthesis of High Intrinsic Loss Power Aqueous Ferrofluids of Iron Oxide Nanoparticles by Citric Acid-Assisted Hydrothermal-Reduction Route. *J. Solid State Chem.* **2012**, *187*, 20−26.

(22) Wei, J.; Liang, Y.; Hu, Y.; Kong, B.; Zhang, J.; Gu, Q.; Tong, Y.; Wang, X.; Jiang, S. P.; Wang, H. Hydrothermal Synthesis of Metal−Polyphenol Coordination Crystals and Their Derived Metal/N-Doped Carbon Composites for Oxygen Electrocatalysis. *Angew. Chem.* **2016**, *128*, 12658−12662.

(23) Hynes, M. J.; Coinceanainn, M. Ó. The Kinetics and Mechanisms of the Reaction of Iron(III) with Gallic Acid, Gallic Acid Methyl Ester and Catechin. *J. Inorg. Biochem.* **2001**, *85*, 131−142.

(24) Fazary, A. E.; Taha, M.; Ju, Y. H. Iron Complexation Studies of Gallic Acid. *J. Chem. Eng. Data* **2009**, *54*, 35−42.

(25) Testa-Anta, M.; Ramos-Docampo, M. A.; Comesaña-Hermo, M.; Rivas-Murias, B.; Salgueiriño, V. Raman Spectroscopy to Unravel the Magnetic Properties of Iron Oxide Nanocrystals for Bio-Related Applications. *Nanoscale Advances*; Royal Society of Chemistry, 2019; pp 2086−2103.

(26) Jin, D.; Kim, H. Magnetization of Magnetite Ferrofluid Studied by Using a Magnetic Balance. *Bull. Korean Chem. Soc.* **2013**, *34*, 1715−1721.

(27) Körner, P.; Jung, D.; Kruse, P. A. Influence of the PH Value on the Hydrothermal Degradation of Fructose. *ChemistryOpen* **2019**, *8*, 1109−1120.

(28) Esposito, D.; Antonietti, M. Chemical Conversion of Sugars to Lactic Acid by Alkaline Hydrothermal Processes. *ChemSusChem* **2013**, *6*, 989−992.

(29) Fazlzadeh, M.; Rahmani, K.; Zarei, A.; Abdoallahzadeh, H.; Nasiri, F.; Khosravi, R. A Novel Green Synthesis of Zero Valent Iron Nanoparticles (NZVI) Using Three Plant Extracts and Their Efficient Application for Removal of Cr(VI) from Aqueous Solutions. *Adv. Powder Technol.* **2017**, *28*, 122−130.
(30) Huang, L.; Weng, X.; Chen, Z.; Megharaj, M.; Naidu, R. Green Synthesis of Iron Nanoparticles by Various Tea Extracts: Comparative Study of the Reactivity. *Spectrochim. Acta, Part A* **2014**, *130*, 295−301.
(31) Li, Z.; Chanéac, C.; Berger, G.; Delaunay, S.; Graff, A.; Lefèvre, G. Mechanism and Kinetics of Magnetite Oxidation under Hydrothermal Conditions. *RSC Adv.* **2019**, *9*, 33633−33642.
(32) Pawlyta, M.; Rouzaud, J. N.; Duber, S. Raman Microspectroscopy Characterization of Carbon Blacks: Spectral Analysis and Structural Information. *Carbon* **2015**, *84*, 479−490.
(33) Sadezky, A.; Muckenhuber, H.; Grothe, H.; Niessner, R.; Pöschl, U. Raman Microspectroscopy of Soot and Related Carbonaceous Materials: Spectral Analysis and Structural Information. *Carbon* **2005**, *43*, 1731−1742.
(34) Herzer, G. Modern Soft Magnets: Amorphous and Nanocrystalline Materials. *Acta Mater.* **2013**, *61*, 718−734.
(35) Bitoh, T.; Makino, A.; Inoue, A.; Masumoto, T. Random Anisotropy Model for Nanocrystalline Soft Magnetic Alloys with Grain-Size Distribution. *Mater. Trans.* **2003**, *44*, 2011−2019.

https://doi.org/10.1021/acsomega.1c03692
ACS Omega 2021, 6, 29547−29554